Scripta Materialia 177 (2020) 151–156

Contents lists available at ScienceDirect

Scripta Materialia

journal homepage: www.elsevier.com/locate/scriptamat

Effects of $LaAlO_3$ and La_2O_2S inclusions on the initialization of localized corrosion of pipeline steels in NaCl solution

Yanhui Hou[a,b], Gang Xiong[a,b], Linli Liu[a,b], Guangqiang Li[a,b,*], Nele Moelans[c,**], Muxing Guo[c]

[a] The State Key Laboratory of Refractories and Metallurgy, Wuhan University of Science and Technology, Wuhan, China
[b] Key Laboratory for Ferrous Metallurgy and Resources Utilization of Ministry of Education, Wuhan University of Science and Technology, Wuhan, Hubei 430081, China
[c] Department of Materials Engineering, KU Leuven, Leuven, Belgium

ARTICLE INFO

Article history:
Received 25 August 2019
Revised 1 October 2019
Accepted 15 October 2019

Keywords:
Inclusion
Pipeline steel
Galvanic corrosion
First-principles

ABSTRACT

Galvanic coupling theory is traditionally adopted to explain initialization of localized dissolution; however, in present study, the conductivity of $LaAlO_3$ and La_2O_2S inclusions was calculated using first-principles to predict whether galvanic corrosion occurs or not. Further, influences of these inclusions on localized corrosion were examined by scanning electron microscope, energy dispersive spectrometer, electron back scattered diffraction, and immersion experiments. It was found that no galvanic coupling occurred between $LaAlO_3$ and the matrix, and microcrevices are the main responsible for localized corrosion. Except microcrevices, an intrinsic potential difference between La_2O_2S and the matrix also contributes to the initialization of localized corrosion.

© 2019 Acta Materialia Inc. Published by Elsevier Ltd. All rights reserved.

Fine spherical inclusions of rare-earth oxides, rare-earth sulfides, and rare-earth oxysulfides reduce the area of microcrevices, which are the main source of pitting corrosion between the steel matrix and inclusions, and also significantly decrease the pitting-induced sensitivity of steels [1–4]. The average size of these rare-earth elements-modified inclusions is much smaller than that of common inclusions [2,5], but still larger than 1 μm. Therefore, these inclusions possess considerable risks of initiating pitting corrosion.

The potential difference theory is widely used to reveal the mechanism of galvanic pitting corrosion in pipeline steels [6–8]. It is traditionally assumed that the selective dissolution of the steel matrix around inclusions occurs due to the galvanic coupling between inclusions and the matrix. Liu et al. [9], based on current-sensing atomic force microscopy (CS-AFM) results, observed that no galvanic coupling occurred between inclusions and the adjacent steel matrix. It is generally noticed that conductive inclusions are the key agents for galvanic pitting corrosion.

In the present study, the conductivity of $LaAlO_3$ and La_2O_2S inclusions was calculated using first-principle study to decide whether galvanic corrosion occurs in the investigated steel or not. Moreover, the effects of $LaAlO_3$ and La_2O_2S inclusions on localized corrosion of the target steel in NaCl solution were investigated by scanning electron microscope (SEM), energy dispersive spectrometer (EDS), electron back scattered diffraction (EBSD), and immersion experiments. In previous studies [10,11], the effects of Mn-absorbed inclusions on the nucleation of intragranular acicular ferrite in X80 pipeline steel were investigated. In the present work, the influences of $LaAlO_3$ and La_2O_2S inclusions on the initial stage of localized corrosion of X80 steel in NaCl solution were further studied. Two different amounts of lanthanum were added to molten X80 pipeline steel. The chemical composition of the investigated steels is presented in Table 1.

In order to simulate the marine environment, immersion experiments were carried out in 3.5% NaCl solution with a pH value of 5.78 at (35 ± 1) °C. The compositions and morphology of inclusions in the samples before and after corrosion were observed by field emission scanning electron microscopy (FE-SEM) and X-ray energy spectrometry.

The Vienna ab-initio simulation package (VASP) [12] (a density functional theory (DFT) software) was employed for the calculations of band structure, surface energy, and work function, and periodic boundary conditions were adopted for this purpose. For band structure calculations, the ultrasoft pseudopotential was used

* Corresponding author at: The State Key Laboratory of Refractories and Metallurgy, Wuhan University of Science and Technology, Wuhan, China.
** Corresponding author at: Department of Materials Engineering, KU Leuven, Leuven, Belgium.
E-mail addresses: houyanhui@wust.edu.cn (Y. Hou), liguangqiang@wust.edu.cn (G. Li), nele.moelans@kuleuven.be (N. Moelans).

https://doi.org/10.1016/j.scriptamat.2019.10.025
1359-6462/© 2019 Acta Materialia Inc. Published by Elsevier Ltd. All rights reserved.

Table 1
Chemical composition of the investigated steels (mass%).

Samples	C	T. O	T. N	Si	Mn	Cr	Ni	Mo	Cu	Ti	Al_s	S	La
1	0.048	0.0031	0.002	0.23	1.78	0.20	0.18	0.17	0.019	0.013	0.050	0.0009	–
2	0.057	0.0029	0.002	0.23	1.76	0.20	0.19	0.17	0.018	0.015	0.054	0.0010	0.0015
3	0.068	0.0020	0.002	0.23	1.80	0.20	0.18	0.16	0.018	0.014	0.067	0.0008	0.0150

*T.O, T. N: Total oxygen and nitrogen content, respectively, including oxygen or nitrogen in inclusions and dissolved in steel matrix; Al_s: Acid-soluble aluminum.

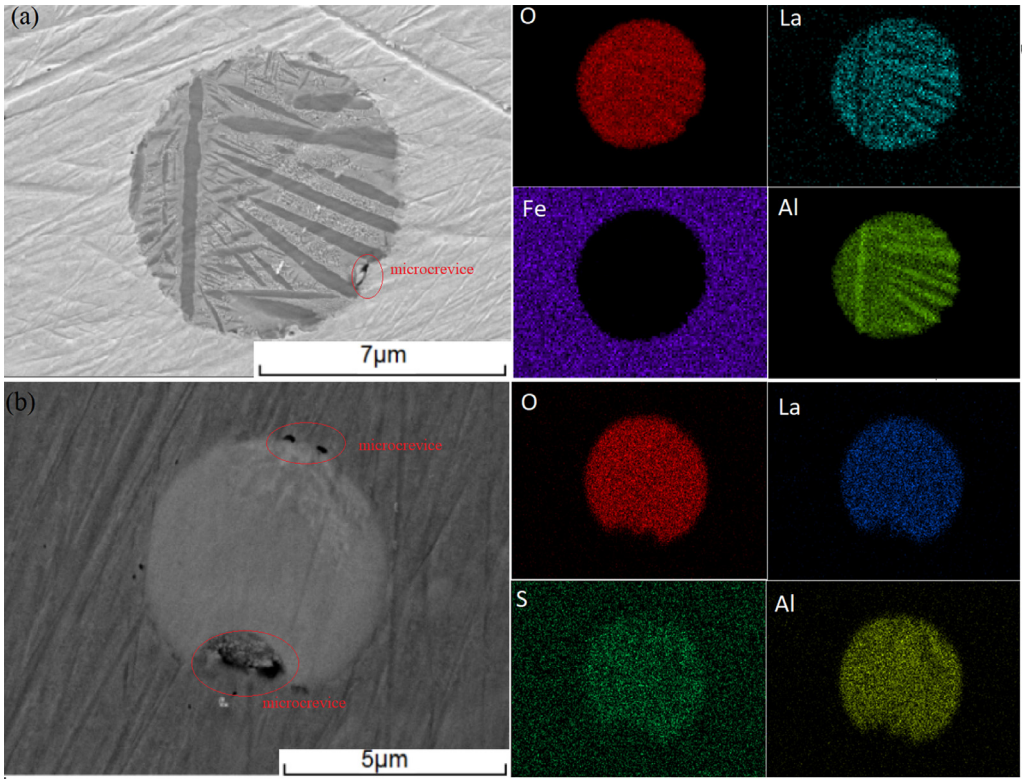

Fig. 1. Morphology and element distribution of two characteristic inclusions. (a) The characteristic inclusions in No. 2 specimen; (b) The characteristic inclusions in No. 3 specimen.

to describe the interactions between real ions and valence electrons. The number of K-point grids was $7 \times 7 \times 7$, and the cut-off energy was set to 500 eV. Further, for the calculations of surface energy and work function, the interactions between valence electrons and ions were described by the projector-augmented wave (PAW) method [13], and a $3 \times 3 \times 1$ k-point grid was selected for this purpose. The Gaussian smearing method with a smearing width of 0.1 eV and cut-off kinetic energy of 350 eV was used to determine electron occupancy. The atomic relaxation was sufficient, and when the maximum value of the inter-atomic force was less than 0.1 eV/nm, relaxation stopped. The Fe matrix possessed a bode-centered cubic (BCC) crystal structure. For the $LaAlO_3$ crystal structure, the space group was R-3c (167), the atomic positions of Al, La, and O were (0, 0, 0), (0, 0, 0.250), and (0.454, 0, 0.250), respectively, and lattice parameters (in Å) were $a = b = 5.370$, $c = 13.100$, $\alpha = \beta = 90°$, and $\gamma = 120°$ [14]. For the La_2O_2S crystal structure, the space group was P–3m1 (164), the atomic positions of La, O, and S were (0.333, 0.667, 0.278), (0.333, 0.667, 0.630), and (0, 0, 0), respectively, and lattice parameters (in Å) were $a = b = 4.040$, $c = 6.920$, $\alpha = \beta = 90°$, and $\gamma = 120°$ [15]. Magnetic properties are considered for the matrix.

Symmetrical crystal planes with periodic conditions and different termination planes on the same crystal plane of the investigated inclusions were used to calculate electronic work functions (W) and potential differences (ΔU) between inclusions and the matrix. The electron work function (W) is defined as the difference between the vacuum level (E_{Vac}) and the Fermi level (E_F) of a material [16]. Therefore,

$$W = E_{Vac} - E_F \tag{1}$$

The electronic potential difference between inclusions and the Fe matrix was calculated based on the smallest surface energy-possessing termination plane of the Fe (100) surface. The intrinsic potential difference (ΔU) between inclusions and the steel matrix was calculated by Eq. (2) [17,18]

$$\Delta U = (W_{incl} - W_{Fe})/e \tag{2}$$

where W_{incl} and W_{Fe} are the work functions of the inclusions and BCC-Fe matrix, and e is the electronic charge.

The formation of $ReAlO_3$ inclusions can be explained by thermodynamic calculations in [19,20]. Combining with the formation sequence analysis [21] and the atomic ratio analysis of inclusions, it is found that the typical inclusions in No. 2 sample are composite inclusions consisting of Al_2O_3 (in rich) and $LaAlO_3$ (in poor) Fig. 1(a)), and the typical inclusions in No. 3 sample are $LaAlO_3$ (in rich) and La_2O_2S (in poor) composite inclusions (Fig. 1(b)). It can be observed in Fig. 1 that microcrevices existed at precipitation intersections and sharp corners of La–Al–O and La–Al–O–S inclusions. They are caused by stress concentrations generated during cooling in the steelmaking process, due to the different thermal

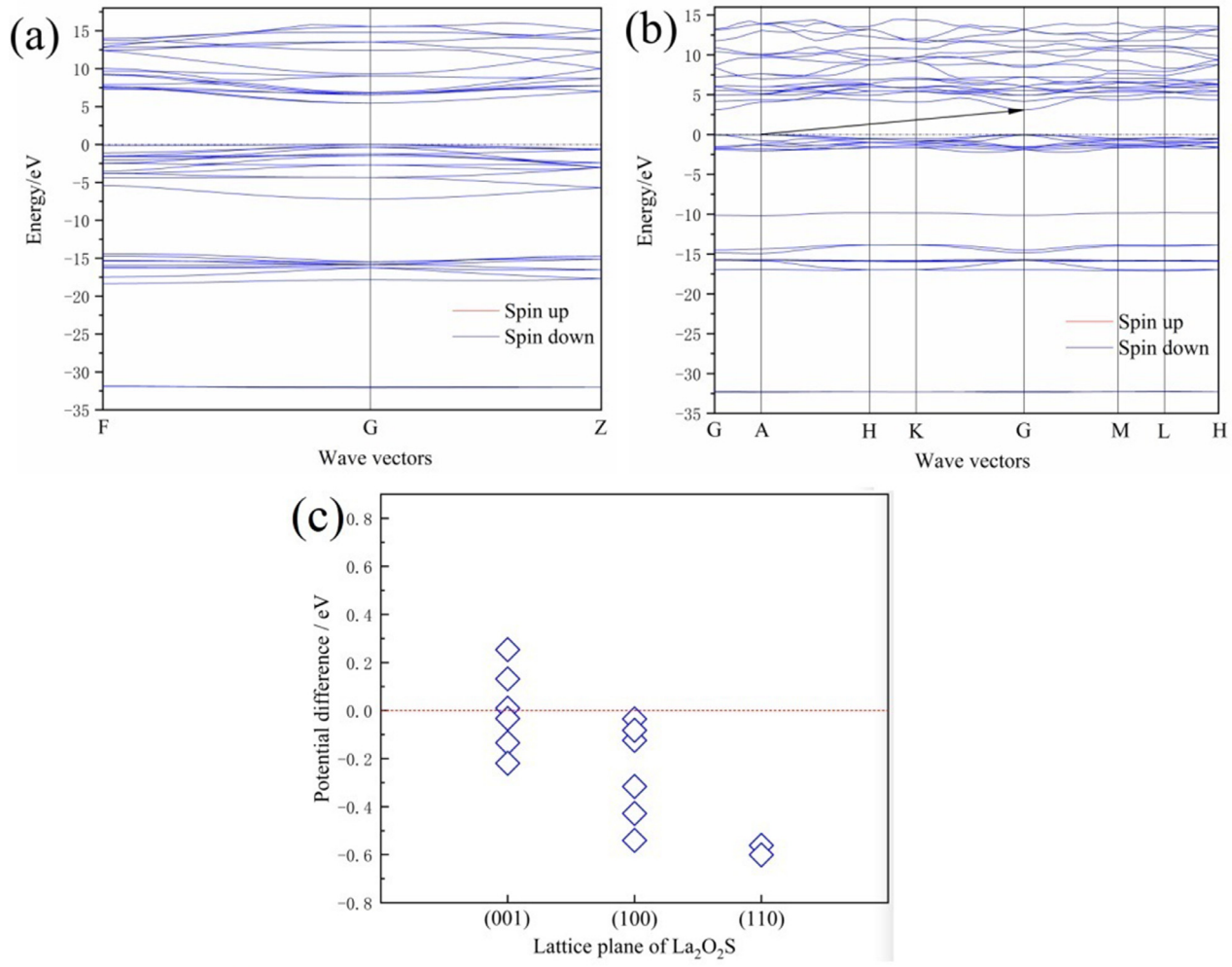

Fig. 2. Energy band structure of (a) $LaAlO_3$ (b) La_2O_2S, and (c) Potential difference between La_2O_2S inclusion and steel matrix. The dotted line for a potential difference equal to 0 eV indicates that the potential difference is based on the work function (4.682 eV) of the matrix crystal plane (100) with the smallest surface energy.

expansion coefficients and different compressive strength or tensile strength between the phases and the matrix.

Galvanic corrosion generally occurs due to the direct contact of heterogeneous conductive materials of different corrosion potentials, thus resulting in local corrosion at contact sites. A material with a low corrosion potential acts as the anode phase, whereas a material with a high corrosion potential serves as the cathode phase. Therefore, the conductivity of $LaAlO_3$ and La_2O_2S inclusions were calculated from their energy band structures (Fig. 2). The bandgap (Eg) of $LaAlO_3$ was calculated as 5.470 eV (Fig. 2(a)), which is slightly lower than the experimental value of 5.6 eV [22]. In general, materials with Eg greater than 5 eV belong to insulators; therefore, it can be considered that $LaAlO_3$ is not conductive and does not contribute to galvanic corrosion. The bandgap of La_2O_2S (3.106 eV) was found to be much narrower than that of $LaAlO_3$ (Fig. 2(b)). Moreover, its conduction band bottom ($E_{C\text{-}min}$) and valence band top ($E_{V\text{-}max}$) were located at different reciprocal space points; hence, La_2O_2S acts as a typical semiconductor material. The bandgap of Al_2O_3 was calculated as 6.154 eV; therefore, Al_2O_3 can also be considered to act as an insulator.

Therefore, the combination of La_2O_2S inclusions in an Fe-rich matrix satisfies the conditions required for galvanic corrosion. The calculated electronic work functions of (001), (100), and (110) surfaces of La_2O_2S are presented in Table 2.

The potential differences between different lattice planes of La_2O_2S and the Fe matrix were obtained by Eq. (2) (Fig. 2(c)) and

Table 2
Work function of La_2O_2S phase for different terminated planes.

Surface	Terminated plane	*W*/eV	Surface	Terminated plane	*W*/eV
	1	4.692		1	4.647
	2	4.814		2	4.142
001	3	4.548	100	3	4.558
	4	4.463		4	4.600
	5	4.649		5	4.254
	6	4.936		6	4.366
110	1	4.121			
	2	4.081			

the (100) matrix termination plane with the lowest surface energy ($W = 4.682$ eV) was selected as the reference structure. It is noticeable from Fig. 2 that the surface potential difference between the (110) plane of La_2O_2S with different terminations and the Fe matrix was about –0.60 eV, which is significantly lower than that of the steel matrix. Hence, from the perspective of galvanic corrosion, when these planes are exposed to a corrosive medium, they act as the anode, dissolving first, while the Fe matrix serves as the cathode. The surface potential differences of the 1st, 3rd, and 4th terminal planes of the La_2O_2S (100) surface were in the range of –0.03 to –0.12 eV; hence, when these planes are exposed to the electrochemical environment, they manifest little effects on corrosion initiation. However, as the surface potentials of the 2nd, 5th, and 6th terminal planes of the La_2O_2S (100) surface were in the range

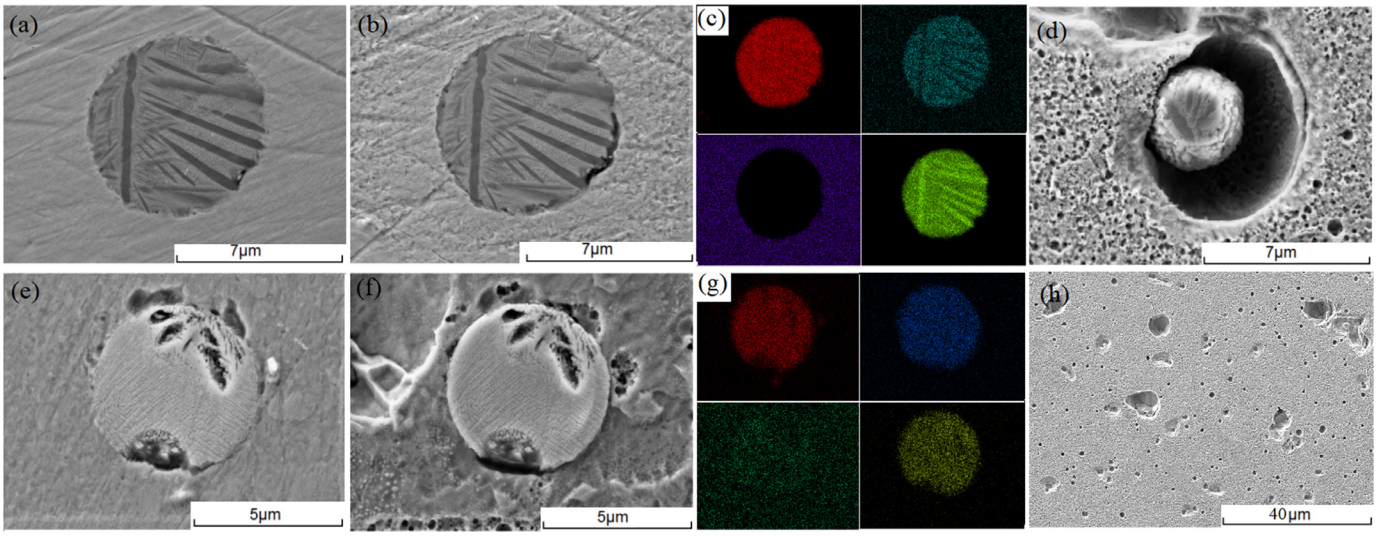

Fig. 3. SEM photographs of No.2 steel corroded in 3.5 wt.% NaCl solution at (a) 10 min, (b) 20 min and (d) 80 min; SEM photographs of No. 3 steel corroded in 3.5 wt.% NaCl solution at (e) 10 min, (f) 20 min, and (h) 80 min. (c) and (g) are the corresponding EDS map of (b) and (f), respectively.

of –0.30 to –0.50 eV, they tend to be dissolved quickly in NaCl solution. The surface potential differences of the corresponding termination planes of the La_2O_2S (001) surface ranged between –0.22 eV and 0.25 eV. The surface potential differences of the 1st, 2nd, 3rd, and 5th termination planes of the La_2O_2S (001) surface were in the range of –0.10 eV to 0.10 eV, thus these planes have little effect on corrosion initiation. The surface potential of the 6th terminal plane of the La_2O_2S (001) surface was about 0.250 eV; hence, when this place is exposed to the corrosive environment, it acts as the cathode, while the Fe matrix dissolves as the anode phase. The surface potential of the La_2O_2S (001)–4th termination plane was about –0.22 eV; thus when this plane is exposed to the corrosive medium, it acts as the anode due to its low surface potential. Therefore, it is evident that most of the surface potential differences for La_2O_2S lattice planes are negative, therefor resulting in localized corrosion.

Fig. 3 displays SEM images of the test specimens after corrosion for different periods. It is observed in Fig. 3(a) that after 10 min immersion, the microcrevices between inclusions and the steel matrix became deeper. After 20 min immersion, the steel matrix near the microcrevices was further corroded and dissolved. Fig. 3(c) exhibits the EDS map corresponding to Fig. 3(b). One can see that inclusions and the steel matrix became completely separated due to the dissolution of the steel matrix. Moreover, when no microcrevices were formed between the inclusion and the steel matrix, inclusions seem to have little effect on pitting initiation. However, when the specimen was immersed for 80 min, pits propagated deeply in the vertical direction due to the simultaneous dissolution of the matrix and inclusions (Fig. 3(d)).

When there are microcrevices around $LaAlO_3$ inclusions, corrosion ions will accumulate in these microcrevices [23], which results in the breakdown of passive film. The mechanism of breakdown of various metal passivation films by Cl^- ions was studied in [24]. As a result of the rupture of passivation film, fresh metal is directly exposed to corrosion solution and in active dissolution state. The steel matrix acts as an anode, and the passivation film acts as a cathode because of its negative potential [3]:

$$Fe \rightarrow Fe^{2+} + e^- \quad (3)$$

$$O_2 + H_2O + e^- \rightarrow OH^- \quad (4)$$

Fe was dissolved continuously and produced Fe^{2+} ions, which reacted with OH^- to form a $Fe(OH)_2$ corrosion product film. Corrosion products are easy to accumulate and cover pitting corrosion holes. Ions with larger radius (such as Fe^{2+}, O^{2-}, etc.) are difficult to shuttle freely through the corrosion product layer, thus catalytic sealing units are formed.

In this sealing unit, oxygen concentration dropped sharply due to poor convection. The enclosed pitting solution was rich with corrosive Cl^- ions with smaller radius, which reacted with cations in the corrosion product film to form soluble chlorides [25].

$$Fe + Cl^- + H_2O \leftrightarrow [FeCl(OH)]^- + H + e^- \quad (5)$$

$$[FeCl(OH)]^- \rightarrow FeCl(OH) + e^- \quad (6)$$

$$FeCl(OH) + H^+ \rightarrow Fe^{2+} + Cl^- + H_2O \quad (7)$$

In the enclosed unit, H^+ ions were continuously produced by the hydrolysis of metal ions. The decrease in pH degree of the pitting solution led to the dissolution of La–Al–O:

$$LaAlO_3 + H^+ \rightarrow La^{3+} + Al^{3+} + H_2O \quad (8)$$

$$Al_2O_3 + H^+ \rightarrow Al^{3+} + H_2O \quad (9)$$

With the decrease of pH value and the increase of corrosive anions such as Cl^-, the corrosion dissolution rate of the steel matrix in the pitting corrosion hole are further accelerated.

It is noticeable from Fig. 3(e) that inclusions existing near microcrevices started to corrode after 10 min immersion and promoted galvanic coupling. After 20 min immersion, corrosion pits were formed on the sample surface (Fig. 3(f)). It is evident from Fig. 3(g) that La_2O_2S inclusions in La–Al–O–S composite inclusions were dissolved due to their weak stability. It is already mentioned that $LaAlO_3$ and La_2O_2S were the characteristic inclusions in No. 3 sample. It was difficult for $LaAlO_3$ to dissolve completely before the formation of the catalytic sealing unit; hence, the steel matrix became severely corroded after 20 min immersion. After 80 min immersion, almost all inclusions fall off (Fig. 3(h)).

Fig. 4 displays EBSD images of two regions containing two typical inclusions in No. 2 and No. 3 samples. Fig. 4(a) and (c) presents FE-SEM images of these two regions, whereas Fig. 4(b) and (d) is the kernel average misorientation (KAM) maps of these regions.

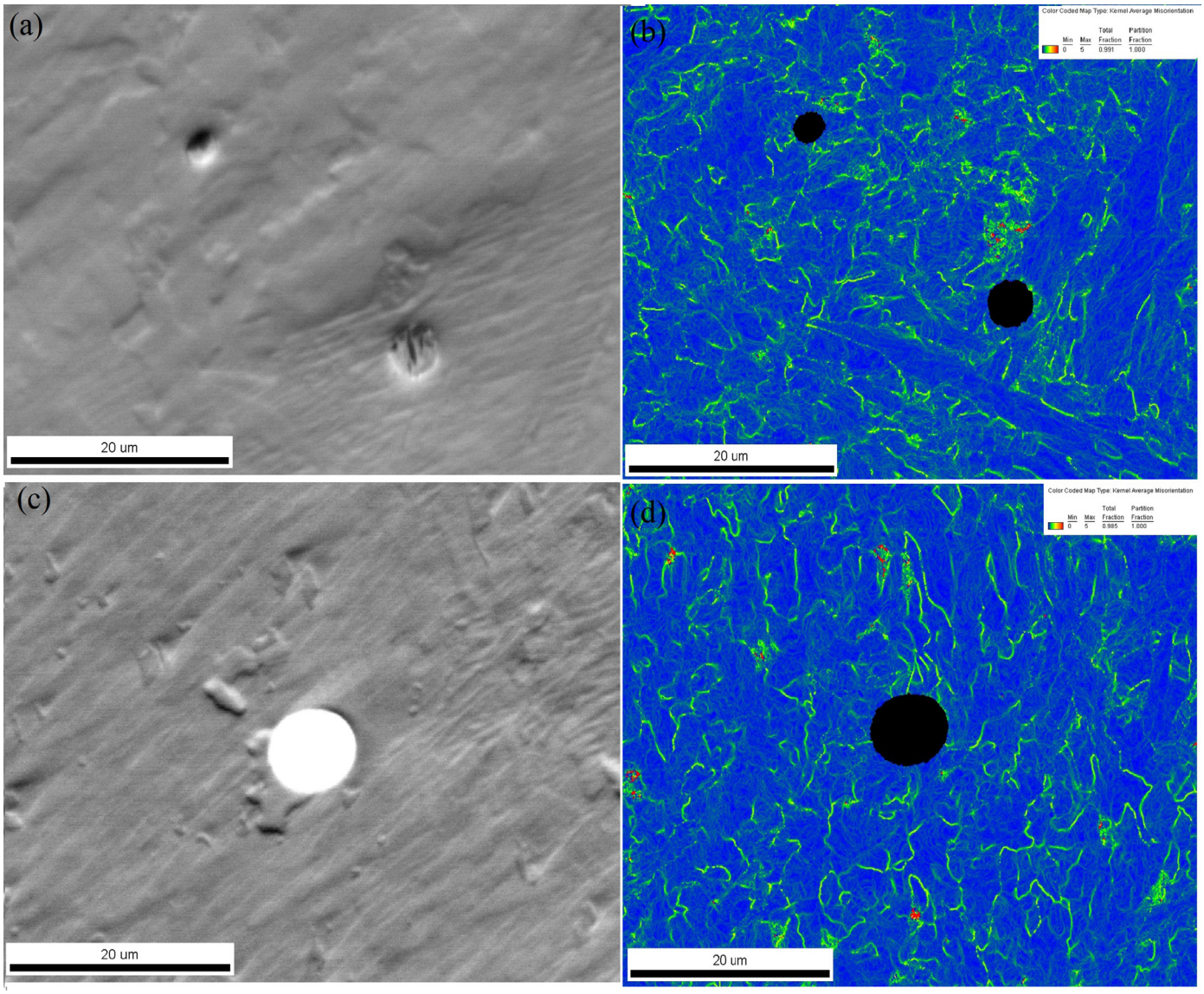

Fig. 4. EBSD images of a region of No.2 steel :(a) FE-SEM image; (c) KAM map of the same region shown in panel (a); and No. 3 steel:(b) FE-SEM image; (d) KAM map of the same region shown in (b).

The average misorientation around La–Al–O and La–S–Al–O inclusions was very small, therefore, it's not the main factor inducing pitting corrosion. This feature is different from that of Al_2O_3 inclusions in [9], since a high deformation was noticed there around the Al_2O_3 inclusions. Hence, it is an important factor explaining the enhanced corrosion resistance of steels alloyed with rare-earth elements.

In summary, no galvanic coupling occurred between $LaAlO_3$ inclusions and the steel matrix, and microcrevices were the key agent for the localized corrosion. In the later stage of pitting corrosion, the decrease in the pH degree of the pitting solution due to the hydrolysis of metal ions in the catalytic sealing pitting unit led to an enhanced $LaAlO_3$ dissolution. La_2O_2S inclusions, in comparison to $LaAlO_3$, manifested a greater impact on pitting corrosion. According to DFT calculations, nearly all surface potentials of different terminal planes of La_2O_2S are negative; hence, La_2O_2S inclusions acted as the anode and were preferentially dissolved in the corrosive environment. Therefore, except microcrevices, the intrinsic potential difference between La_2O_2S inclusions and the Fe matrix contributed to localized corrosion.

Declaration of Competing Interest

The authors declare that they have no known competing financial interests or personal relationships that could have appeared to influence the work reported in this paper.

Acknowledgment

This work is supported by Key Project of the State Key Laboratory of Refractories and Metallurgy for Young Scientists, Project of the Key Laboratory for Ferrous Metallurgy and Resources Utilization of Ministry of Education, and Scientific Research Foundation for the Returned Overseas Chinese Scholars.

References

[1] H.Y. Ha, C.J. Park, H.S. Kwon, Scr. Mater. 55 (2006) 991.
[2] S.H. Jeon, S.T. Kim, M.S. Choi, J.S. Kim, K.T. Kim, Y.S. Park, Corros. Sci. 75 (2013) 367.
[3] C. Liu, R.I. Revill, Z.Y. Liu, D.W. Zhang, X.G. Li, H. Terryn, Corros. Sci. 129 (2017) 82.
[4] Y. Watanabe, V. Kain, T. Tonozuka, T. Shoji, T. Kondo, F. Masuyama, Scr. Mater. 55 (2006) 991.

[5] S.H. Jeon, S.T. Kim, I.S. Lee, Y.S. Park, Corros. Sci. 52 (2010) 3537.
[6] I. Apachitei, L.E. Fratila-Apachitei, J. Duszczyk, Scr. Mater. 57 (2007) 1012.
[7] Z. Hua, B. An, T. Iijima, C. Gu, J. Zheng, Scr. Mater. 131 (2017) 47.
[8] S. Zheng, C. Li, Y. Qi, L. Chen, C. Chen, Corros. Sci. 67 (2013) 20.
[9] C. Liu, R.I. Revilla, D. Zhang, Z.Y. Liu, Corros. Sci. 138 (2018) 96.
[10] Y.H. Hou, W. Zheng, Z.H. Wu, G.Q. Li, N. Moelans, M.X. Guo, B.S. Khan, Acta Mater. 118 (2016) 8.
[11] Z.H. Wu, W. Zheng, G.Q. Li, H. Matsuura, F. Tsukihashi, Metall. Mater. Trans. B 46 (2015) 1226.
[12] G. Kresse, Phys. Rev. B 54 (1996) 11169.
[13] P.E. Blöchl, Phys. Rev. B 50 (1994) 17953.
[14] K. Vidyasagar, J. Gopalakrishnan, C.N.R. Rao, J Solid State Chem. 58 (1985) 29.
[15] D.B.M. Klaassen, H. Mulder, C.R. Ronda, Phys. Rev. B. 39 (1989) 42.
[16] D.P. Ji, Q. Zhu, S.Q. Wang, Surf. Sci. 651 (2016) 137.
[17] C. Larignon, J. Alexis, E. Andrieu, L. Lacroix, G. Odemer, C. Blanc, Scr. Mater. 68 (2013) 479.
[18] Z.L. Hua, S.Y. Zhu, B. An, T. Iijima, C.H. Gu, J.Y. Zheng, Scr. Mater. 162 (2019) 219.
[19] W.G. Wilson, D.A.R. Kay, A. Vahed, JOM 26 (1974) 14.
[20] L.J. Wang, Q. Wang, J.M. Li, K.C. Chou, J. Min. Metall. 52 (2016) 4.
[21] N. Ånmark, A. Karasev. Materials 8 (2015) 751.
[22] S.G. Lim, S. Kriventsov, T.N. Jackson, J.H. Haeni, D.G. Schlom, A.M. Balbashov, R. Uecker, P. Reiche, J.L. Freeouf, G. Lucovsky, J. Appl. Phys. 4500 (2002) 91.
[23] A. Szummer, M. Janik-Czacho, S. Hofmann, Mater. Chem. Phys. 34 (1993) 181.
[24] B. Zhang, J. Wang, B. Wu, X.W. Guo, Y.J. Wang, D. Chen, Y.C. Zhang, K. Du, E.E. Oguzie, X.L. Ma, Nat. Commun. 9 (2018) 1.
[25] I. Rosenfeld, I. Marshakov, Corrosion 115 (1964) 125.